Supplementary Information (SI) for Journal of Materials Chemistry A.

Supplementary Information

Efficient solar-driven electrocatalytic nitrate-to-ammonia by 2D ultrathin Fe single-atomic catalysts

Ji Li,[a,b,*] Weiqi Zhong,[a] Kai Wu,[a] Eddy Petit,[b] Luc Lajaunie,[c,d] Kun Qi,[e] Yang Zhang,[b] Huali Wu,[f] Jiefeng Liu,[b] Jing Heng,[a] Xuechuan Wang,[a] Qingxin Han,[a] Taotao Qiang,[a] Damien Voiry [b,*]

[a] College of Bioresources and Materials Engineering, Shaanxi University of Science & Technology, Xi'an 710021, PR China

[b] Institut Europeen des Membranes, IEM, UMR 5635, Université Montpellier, ENSCM, CNRS, 34095 Montpellier Cedex 5, France

[c] Departamento de Ciencia de los Materiales e Ingeniería Metalúrgicay Química Inorgánica, Facultad de Ciencias, Universidad de Cádiz, Campus Río San Pedro S/N, Puerto Real, 11510, Cádiz, Spain

[d] Instituto Universitario de Investigación de Microscopía Electrónicay Materiales (IMEYMAT), Facultad de Ciencias, Universidad de Cádiz, Campus Río San Pedro S/N, Puerto Real 11510, Cádiz, Spain

[e] Chinese Academy of Sciences Dalian Institute of Chemical Physics, Dalian, 116023, PR China

[f] Southwest Jiaotong University, Research Institute of Frontier Science, Chengdu, Sichuan, 610031, PR China

[*] Corresponding author: College of Bioresources and Materials Engineering, Shaanxi University of Science & Technology, Xi'an 710021, PR China

Institut Europeen des Membranes, IEM, UMR 5635, Université Montpellier, ENSCM, CNRS, 34095 Montpellier Cedex 5, France

E-mail address:liji@sust.eud.cn(Ji Li)

damien.voiry@umontpellier.fr (Damien Voiry)

Materials. Iron(III) nitrate nonahydrate ($Fe(NO_3)_3·9H_2O$) and salicylic acid (SA), ammonium chloride (NH_4Cl), sodium citrate dihydrate, sodium nitroferricyanide dihydrate, sodium hypochlorite solution, HCl, KNO_3, $K^{15}NO_3$, and ^{15}N labeled ammonium chloride ($^{15}NH_4Cl$) were purchased from Sigma-Aldrich (France). 2-Methyl-imidazole (2-MeIm, 98%), methanol, and sodium chloride (NaCl), Nafion (5%) were purchased from Alfa Aesar. All the reagents were used as received without further purification. The water used throughout all experiments was purified through a Millipore system.

Catalysts Synthesis. The 2D ZIF-8 and Fe-doped ZIF-8 nanosheets were synthesized as previously described with some modifications.[1] Take 2D Fe-SAC-10 as an example, 50 mg of $Zn(NO_3)_2·6H_2O$ and 50 mg of $Fe(NO_3)_3·9H_2O$ were dissolved in 6 mL of methanol. And 200 mg of 2-MeIm was dissolved into another 6 mL of methanol. Then the solutions above mentioned were successively added into a 250 mL beaker, which contained 30 g of ground NaCl powder, with vigorous magnetic stirring overnight at ambition temperature. Subsequently, the solvent of methanol was removed by a slowly evaporating process at 35 °C. Then, the as-prepared NaCl@ZIF-8 and NaCl@Fe-ZIF-8 nanosheets were pyrolyzed under 900 °C with a ramping rate of 5 °C

min^{-1} in a tube furnace and kept at 900 °C with flowing Ar for 120 min to obtain 2D NC and 2D Fe-SAC-50. The as-prepared 2D Fe-SAC-10 was immersed in 0.5 M of H_2SO_4 for 24 h to remove the Fe nanoparticles and unstable substances and then resined at least 3 times with water to remove the NaCl and remaining acid. Finally, the catalyst was dried at 65 °C overnight. The Fe atom loading amount was controlled by changing $Fe(NO_3)_3 \cdot 9H_2O/Zn(NO_3)_2 \cdot 6H_2O$ mass ratios from 0/5, 1/5, 2/5, 3/5, 4/5, to 5/5, the sample were referred to as 2D Fe-SACs-x, the x represents the mass of $Fe(NO_3)_3 \cdot 9H_2O$ in the feeding solution. The three-dimensional Fe-SAC (3d Fe-SAC) was synthesized by the same method in the absence of NaCl powder. In terms of mesoporous Fe SAC (M-Fe-SAC), it was synthesized by polymerization and a pyrolysis process in the presence of the SBA-15 template.[40] In brief, 500 mg of aniline, 7.5 g of SBA-15 (40 wt%), and 147 mg of $FeCl_3$ were dispersed into 10 mL 1.0 M HCl. Subsequently, 2.5 g of the initiator that composed of 1.0 M HCl solution and 1.25 g ammonium peroxydisulfate (APS) was added dropwise slowly into the above-mentioned solution with vigorous stirring in an ice bath for 24h. Then, the as-obtained SiO_2@PANI-Fe was pyrolyzed with a ramping rate of 5 °C min^{-1} in a tube furnace and kept at 900 °C with flowing Ar gas for 120 min after removing the water by evaporation. The SBA-15 and unstable metal species were etched by HF (10wt. %) etching. Finally, the mesoporous Fe SAC was dried at 65 °C overnight.

Physical characterizations. The morphology of as-prepared catalysts was observed using FEI Talos F200X TEM. Powder XRD patterns were recorded by a PANalytical X' pert Pro diffractometer using a Cu Kα source ($\lambda = 0.154178$ nm). X-ray photoelectron spectrum (XPS) was measured on a Thermo ESCALAB 250XI using monochromatic Al Kα radiation. All binding energies of the spectra were referenced to the C 1s peak set at 284.6 eV. The chemical structures were characterized by Invia Raman Microscope (Renishaw, United Kingdom) under an excitation of 633 nm laser light. X-ray absorption spectroscopy (XAS) at the Fe K-edges (E_0=7200 eV) was performed at the SAMBA beamline of the SOLEIL synchrotron radiation facility, using the fluorescence mode. The ultraviolet-visible (UV-Vis) absorbance spectra were recorded on a UV2600 spectrometer (SHIMADZU, Japan). For isotope labeling experiments, the NMR was performed at 25 °C on a Bruker AVANCE III HD spectrometer operating at a 1H frequency of 600 MHz.

Electrochemical Measurements. The electrochemical performance of catalysts for NO_3RR was evaluated both in a three-electrode and two-electrode configuration with a PARSTAT MC potentiostat (AMETEK Inc., USA) in an H-type electrolytic cell separated by Nafion® 117 membrane. For working electrode ink preparation, 5 mg of catalyst was dispersed in 1.0 mL containing 50 μL of Nafion solution (5 wt%) ethanol through sonication for 1 h. Then 50 μL of ink was drop-cast onto graphite foil with a diameter of 11.3 mm. Subsequently, the prepared electrodes were dried in the air under ambient temperature for 12 h. Pt foil and Ag/AgCl electrode with a glass frit were used as the counter and reference electrode in the three-electrode configuration, respectively. The electrolyte in all electrochemical tests was 0.1 M of NaOH presence of 0.1 M $NaNO_3$. And 80 mL of electrolyte was distributed to the cathode and anode compartment. All potentials were referenced to the reversible hydrogen electrode

(RHE) by the equation $E_{\mathrm{RHE}} = E_{\mathrm{Ag/AgCl}}+0.197+0.059\mathrm{pH}$. Before NO_3RR, the cyclic voltammetry (CV) was run 30 cycles at a scan rate of 100mV s^{-1} from 1.023 to -0.997 V to activate the catalyst. For the isotopic experiment, 0.1 M of NaOH presence of 0.1 M $Na^{15}NO_3$ was used as the electrolyte to clarify the source of ammonia. The 0.5 mL of $^{15}NH_4^+$ was quantified by ^{1}H NMR (600 MHz) after mixing with 0.5 mL of D_2O and 50 μL of concentrated H_2SO_4. The linear sweep voltammetry (LSV) curves are recorded at a scan rate of 20 mV s^{-1} from 1.023 to -0.997 V *vs*. RHE. Then, the catalytic performance of each catalyst was tested by a chronoamperometry at different potentials for 30 min. To evaluate the electrochemical specific area, the electrochemical double-layer capacitance (Cdl) method was employed in a potential window without the Faradaic process at increasing scan rates between 20 to 140 mV s^{-1}. A 2.0 ×1.0 cm^2 triple-junction GaAs (InGaP/GaAs/Ge) solar cell (HGSC-A100B-2S, Hasunopto Co., Hongkong) was adopted in the solar-driven electrocatalysis system as the light absorber. The light source was a 450 W xenon lamp (Oriel) equipped with a Schott K113 Tempax sunlight filter (Praezisions Glas & Optik GmbH) to match the emission spectrum of the lamp to the AM1.5G standard. The *J-V* characteristics of the triple-junction solar cell were recorded by a programmed digital source meter (Keithley Model 2400) under the illumination of AM 1.5G (100 mW cm^{-2}). The current and voltage at the maximum power point were 14.10 mA and 4.24 V, respectively, corresponding to the maximum efficiency of 29.89 % under 1 sun irradiation.

Determination of NH_3. The concentration of NH_3 was measured by UV–vis spectrophotometry with the indophenol blue method.[2] In detail, 200 μL electrolyte was taken out from the cathodic chamber and 50 µL of NaClO (ρ_{Cl} = 4–4.9)/NaOH (0.75 M) solution was added. Then, 500 µL of 0.4 M salicylic acid/NaOH (0.32 M), and 50 µL of 1.0% (w/w) $Na_2[Fe(CN)_5NO]\cdot 2H_2O$ solutions were added sequentially. The absorbance of the solution was measured by UV-Vis after 1 h at λ = 660 nm. The Faradaic efficiency of NH_3 (FE(NH_3)) and yield rate of NH_3 (*Y.R*(NH_3)) was calculated using the following Equation 1 and 2:

$$FE(NH_3) = n \times F \times C_{NH3} \times \frac{V}{Q} \times 100\% \#(1)$$

$$Y.R(NH_3) = \frac{C_{NH3} \times V}{t \times S} \#(2)$$

where *n* is the number of transferred electrons (*n* = 8 for electroreduction of NO_3^- to NH_3), *F* is the Faraday constant (C mol^{-1}), C_{NH3} is the concentration of NH_3 in the cathode chamber (M), *Q* is the total charge passing the electrode (i.e. current times electrolysis time, C), *t* is the electrolysis time (s), *S* is the geometric area of the working electrode (cm^2).

Determination of NO_2^-. The NO_2^- concentration was measured by the Griess method[3] using a coloring reagent which is a mixture of p-aminobenzene sulfonamide (4 g), N-(1-Naphthyl) ethylenediamine dihydrochloride (0.2 g), and 10 mL of phosphoric acid in 50 mL of deionized water. In brief, 0.5 mL of electrolyte was taken out and diluted by 5mL of deionized water, then, mixed with 1 mL of the above-mentioned coloring reagent. The absorbance was measured at a wavelength of 540 nm by ultraviolet-visible spectroscopy after sitting for 20 min. The Faradaic efficiency of NO_2^- (FE(NO_2^-)) was calculated using the following Eq.3:

$$FE(NO_2^-) = \frac{2 \times F \times c(NO_2^-) \times V}{Q} \times 100\% \#(3)$$

where C_{NO2-} is the concentration of NO_2^- in the cathode chamber (M), Q and F are the total charge passing the electrode and Faradaic constant.

Determination of H_2. The gas by-product (H_2) were quantified by gas chromatography (GC, 9070II; Fuli). The GC device was equipped with a thermal conductivity detectors for H_2 signal. The GC was carried out using packed columns of two Porapak-N, a Molecular sieve-5A, employing Argon (99.999%) as the carrier gases. 10 μL of gas of cell was injected in GC for H2 determination. The FEs of H_2 were calculated by using the Eq.4:

$$FE(H_2) = \frac{\varphi \times \frac{V_{up}}{22.4} \times 2 \times F}{Q} \times 100\% \#(4)$$

where φ is the volume fraction of H_2, V_{up} is the volume of cell subtact the volume of electrolyte.

Energy conversion efficiency measurement. The energy conversion efficiency of the 2-electrode configuration was calculated for NH_3 by Equation 5:[4]

$$EE(NH_3) = \frac{(1.23 - E^o)FE(NH_3)}{1.23 - E} \times 100\% \#(5)$$

where $E°$ is the equilibrium potential (0.69 V) of nitrate electroreduction to ammonia in alkaline media; $FE(NH_3)$ is the faradaic efficiency of NH_3, and E is the applied potential (vs. RHE) on the cell.

Electric power consumption estimation. The electric power consumption (EPC) represents the amount of electric energy (typically expressed in kWh), that is required for producing 1 kg of product, was calculated for NO_3RR by Equation 6 (for three-electrode configuration) and Equation 7 (for two-electrode configuration) which like the literature:[5]

$$EPC(NH_3) = n \times F \times \frac{1.23 - E}{3600 \times 17 \times FE(NH_3)}\#(6)$$

$$EPC(NH_3) = n \times F \times \frac{V_{in}}{3600 \times 17 \times FE(NH_3)}\#(7)$$

where *n* is the number of transferred electrons (*n* = 8 for electroreduction of NO_3^- to NH_3), 17 is the molecular weight of NH_3, V_{in} is the applied voltage in two-electrode system.

Turnover frequency of ammonia. The turnover frequency (TOF, s^{-1}) in the NO_3RR is defined as the mean number of ammonia molecules produced on an active site of catalyst per second. Therefore, TOF values can be estimated based on the equation 8:[6]

$$TOF = \frac{j_{NH3} \times M_{metal}}{n \times F \times m_{cat} \times \omega}\#(8)$$

where j_{NH3} is the partial current density of ammonia (mA cm^{-2}), *n* is the number of transferred electrons (*n* = 8 for electroreduction of NO_3^- to NH_3), *F* is the Faraday constant (C mol^{-1}), m_{cat} represents the mass of catalyst on the electrode (g); *ω* is the mass fraction of active sites in the catalyst (%), M_{metal} is the atomic mass of metal (Fe: 55.85 g mol^{-1},).

Estimation of the solar-to-Ammonia (STA) conversion efficiency. For the solar-driven electrolysis, the conversion efficiency of solar-to-ammonia (STA) was calculated by Equation 9:[7]

$$STA = E^{\circ} \times I_{op} \times FE(NH_3)/P_{sun}\#(9)$$

where P_{sun} is the power of the sun (100 mW cm^{-2}), I_{op} is the current density per illuminated solar cell area.

Computational detail. All the spin-polarized density functional theory (DFT) calculations were implemented in the Vienna Ab-initio Simulation Package (VASP) code with a projector augmented-wave (PAW) method.[8,9] The exchange-correction energy was described using a generalized gradient approximation (GGA) with a Perdew–Burke–Ernzerhof (PBE) format. A plane-wave basis with a kinetic energy cutoff of 520 eV was chosen to expand the electronic wave functions. The Fe-SAC model was built based on a 5×5×1 monolayer graphene supercell, in which one metal atom was coordinated with 1~4 pyridine nitrogen atoms respectively. A 20 Å vacuum layer above the basal plane was adopted to avoid the interaction between neighboring images. For the geometrical optimizations, all atoms were fully relaxed to the ground state with the convergence of energy and forces setting to 1.0×10^{-5} eV and 0.01 eV $Å^{-1}$, where a 3×3×1 Γ-centered Monkhorst-Pack schemed *k*-mesh was used to sample the first Brillouin zone. The DFT-D2 of Grimme was used for the long-range dispersion correction.[10] To evaluate the NO_3RR performance of each catalyst, the chemical reaction considered can be summarized with the reaction equations below (10-17):

$$* + NO_3^- \rightarrow *NO_3^- + H_2O\#(10)$$

$$*NO_3^- + H_2O + 2e^- \rightarrow *NO_2 + 2OH^-\#(11)$$

$$*NO_2 + H_2O + 2e^- \rightarrow *NO + 2OH^-\#(12)$$

$$*NO + H_2O + e^- \rightarrow *NOH\ (or *NHO) + OH^-\#(13)$$

$$*NOH\ (or *NHO) + H_2O + e^- \rightarrow *NHOH + OH^-\#(14)$$

$$*NHOH + H_2O + e^- \rightarrow *NH + OH^-\#(15)$$

$$*NH + H_2O + e^- \rightarrow *NH_2 + OH^-\#(16)$$

$$*NH_2 + H_2O + e^- \rightarrow *NH_3 + OH^- \#(17)$$

The Gibbs free energy change (ΔG) of the above-mentioned elementary steps was calculated by Eq.18 based on the computational hydrogen electrode (CHE) model proposed by Nørskov et al.[11]

$$\Delta G = \Delta E + \Delta E_{ZPE} - T\Delta S\#(18)$$

where ΔE is the energy difference before and after adsorption for each elementary step. ΔE_{ZPE} and ΔS, respectively, are the difference of the zero-point energy and the vibrational entropy. All data are listed in Table S2. T is the temperature (i.e. 298.15 K).

The ratio of specific area for 2D SACs to 3D SACs

Take the ZIF-8-derived Fe-SACs as an example, the rhombic dodecahedron is a convex polyhedron with 12 congruent rhombic faces. It has 24 edges and 14 vertices of 2 types. It is a Catalan solid and the dual polyhedron of the cuboctahedron. The surface area A_{Rh} and the volume V_{Rh} of the rhombic dodecahedron with edge length a are:

$$A_{Rh} = 8\sqrt{2}a^2\#(19)$$

$$V_{Rh} = 16\sqrt{3}/9a^3\#(20)$$

A nanosheet is a two-dimensional nanostructure with thickness in a scale ranging from 1 to 100 nm. The nanosheet is assumed to be a regular cuboid with a length m, width n and thickness d geometry. The surface area A_{NS} and the volume V_{NS} of nanosheets are, respectively:

$$A_{NS} = 2mn\#(21)$$

$$V_{NS} = mnd\#(22)$$

If we assume that 1 gram of 2D material is made up of N_1 nanosheets, and 1 gram of 3D material consists of N_2 rhombic dodecahedra, both materials having the same density ρ, then we can express their masses using the following equation:

$$M_{2D} = N_1 mnd\rho\#(23)$$

$$M_{3D} = N_2 16\sqrt{3}/9a^3\rho\#(24)$$

Equation 25 provides the expression for the ratio of the surface area of the 2D material to that of the 3D material, denoted as R_s.

$$R_s = 2\sqrt{6}/9a/d\#(25)$$

XAS analysis

The acquired EXAFS data were processed according to the standard procedures using the ATHENA module implemented in the IFEFFIT software packages.[12] The k3-weighted EXAFS spectra were obtained by subtracting the post-edge background from the overall absorption and then normalizing for the edge-jump step. Subsequently, k3-weighted χ(k) data of Fe K-edge were Fourier transformed to real (R) space using a Hanning window (dk=1.0 $Å^{-1}$) to separate the EXAFS contributions from different coordination shells. To obtain the quantitative structural parameters around central atoms, least-squares curve parameter fitting was performed using the ARTEMIS module of IFEFFIT software packages.[13,14]

Supplementary Figures

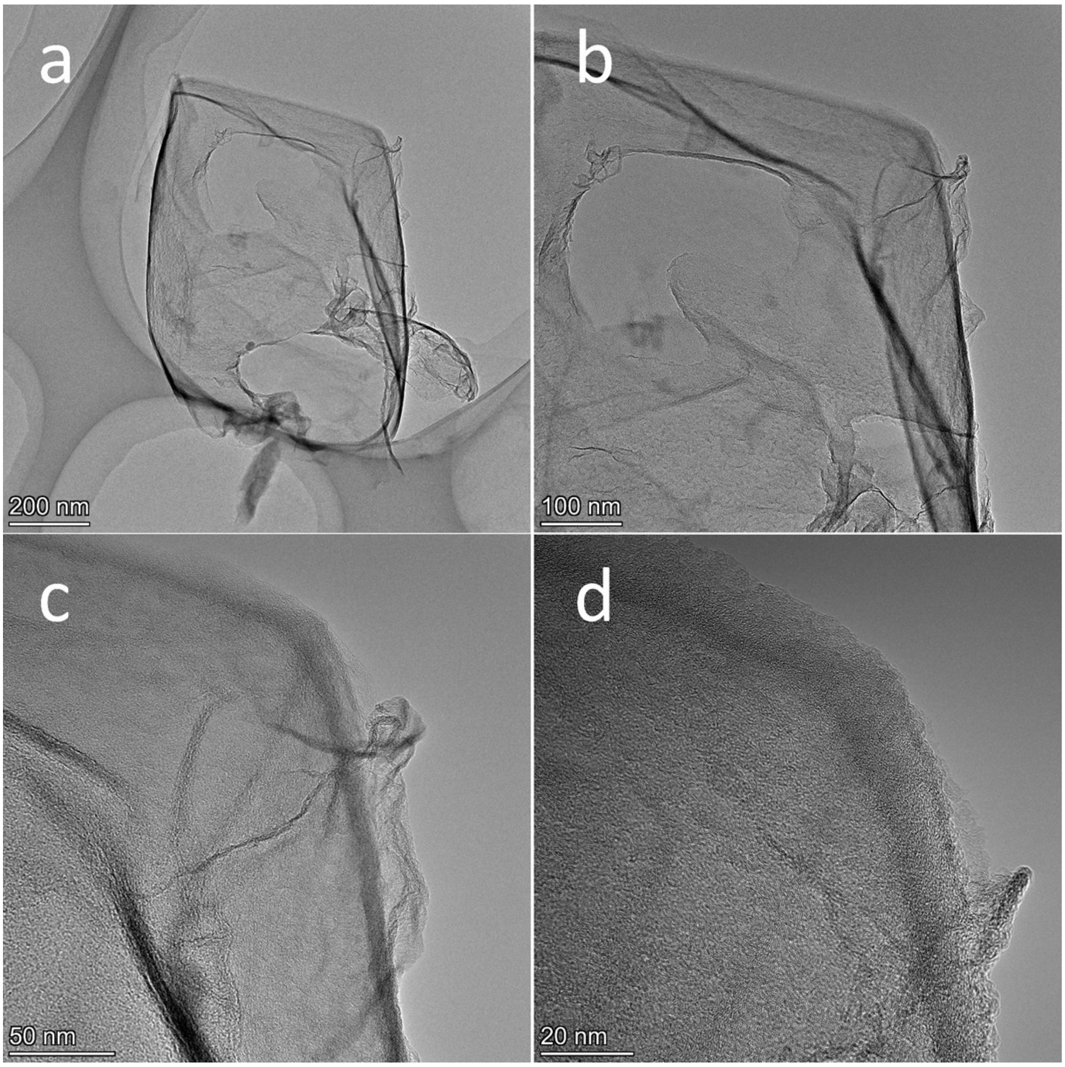

Supplementary Figure S1. TEM (**a, b**) and HRTEM (**c**, **b**) images of 2D Fe-SACs, respectively.

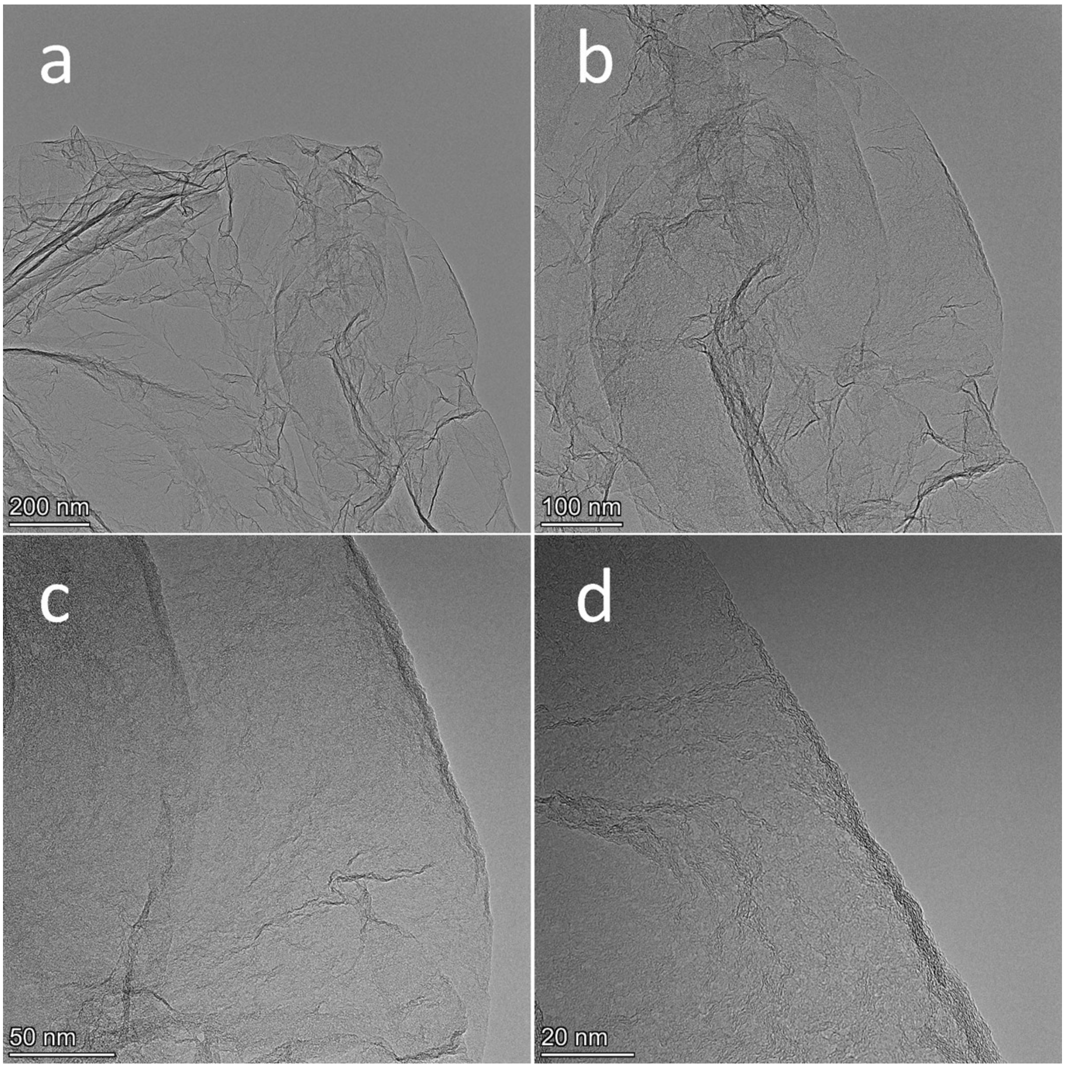

Supplementary Figure S2. TEM (**a, b**) and HRTEM (**c**, **b**) images of 2D NC, respectively.

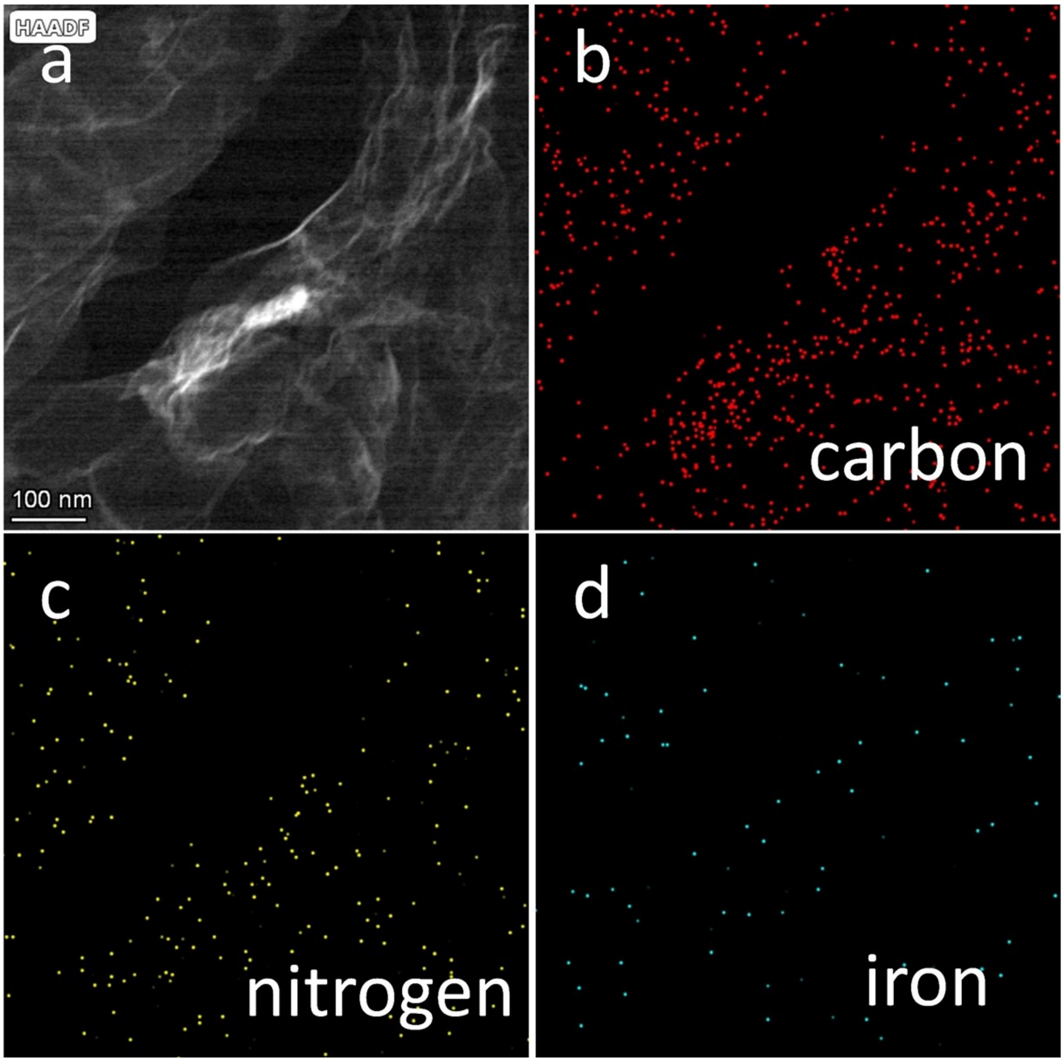

Supplementary Figure S3. High-angle annular dark-field scanning transmission electron microscope (HAADF-TEM) images of 2D Fe-SACs (**a**) and corresponding energy dispersive X-ray (EDX) mapping for Carbon (**b**), nitrogen (**c**), and iron (**d**).

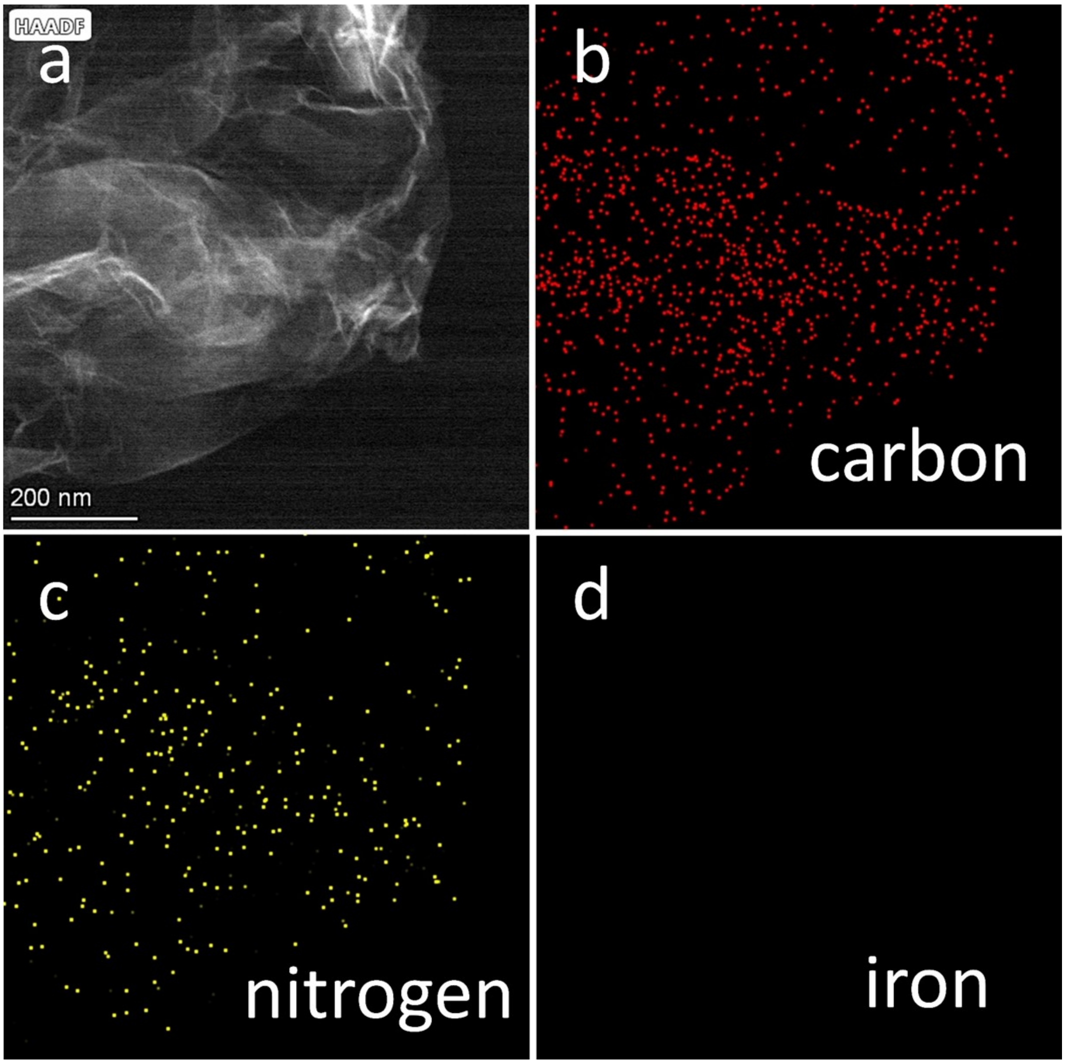

Supplementary Figure S4. High-angle annular dark-field scanning transmission electron microscope (HAADF-TEM) images of 2D NC (**a**) and corresponding energy dispersive X-ray (EDX) mapping for Carbon (**b)**, nitrogen (**c)**, and iron (**d)**.

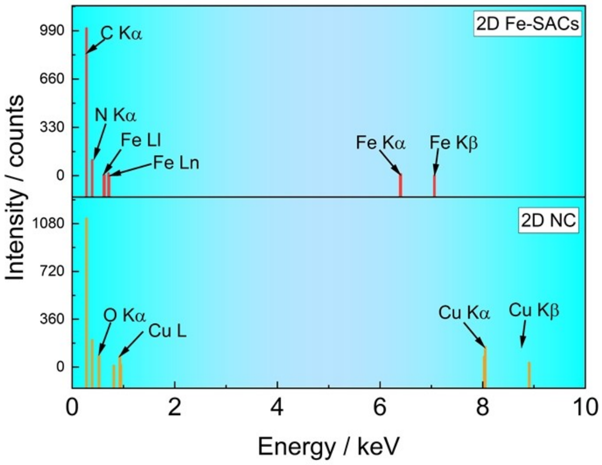

Supplementary Figure S5. EDS results of 2D Fe-SACs and 2D NC.

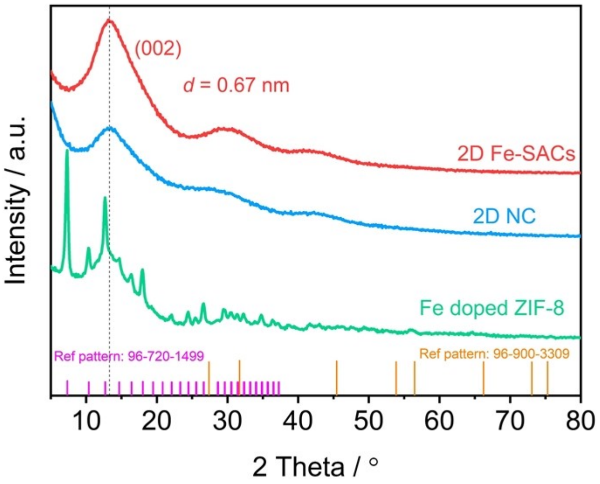

Supplementary Figure S6. X-ray diffraction (XRD) patterns of the 2D Fe-SACs, 2D NC, and Fe-doped ZIF-8 nanosheets, respectively.

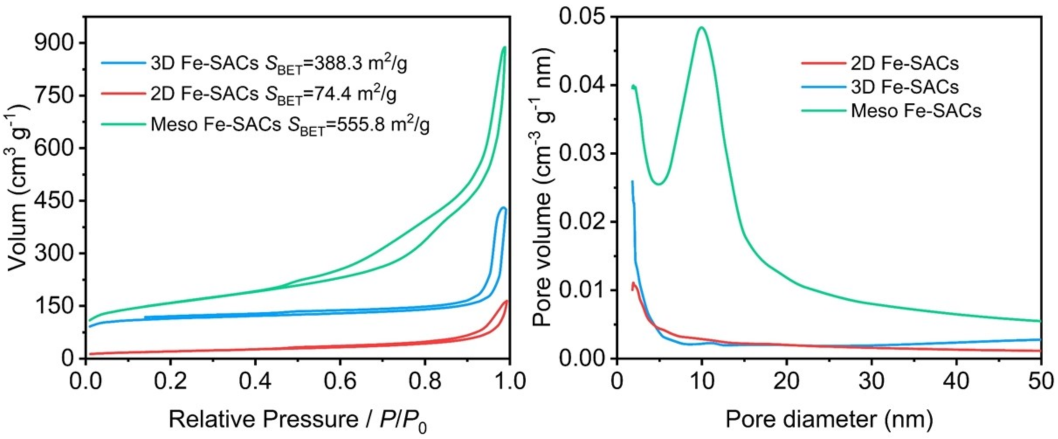

Supplementary Figure S7. BET specific surface area (a) and BJH pore size distribution (b) of 2D Fe-SACs (red line), 3D Fe-SACs (blue line), and Meso Fe-SACs (green line).

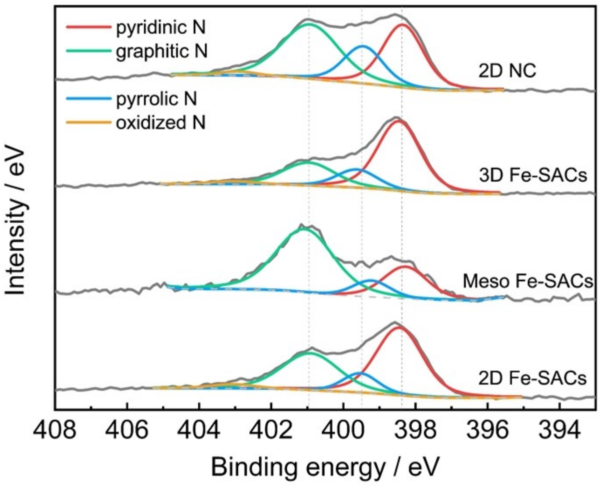

Supplementary Figure S8. High-resolution N1s XPS spectra for 2D Fe-SACs, 3D Fe-SACs, Meso Fe-SACs, and 2D NC, respectively.

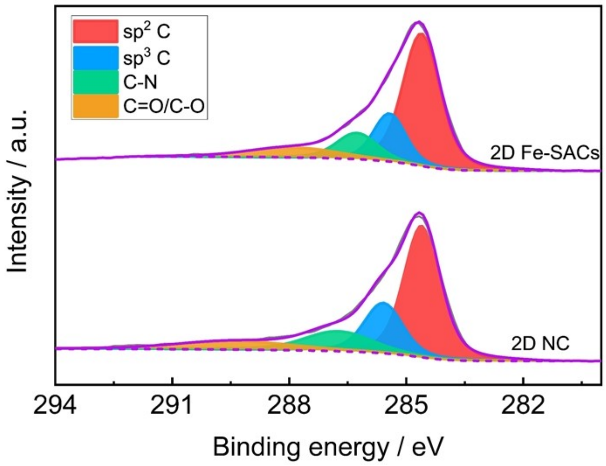

Supplementary Figure S9. High-resolution C1s XPS spectra for 2D Fe-SACs and 2D NC, respectively.

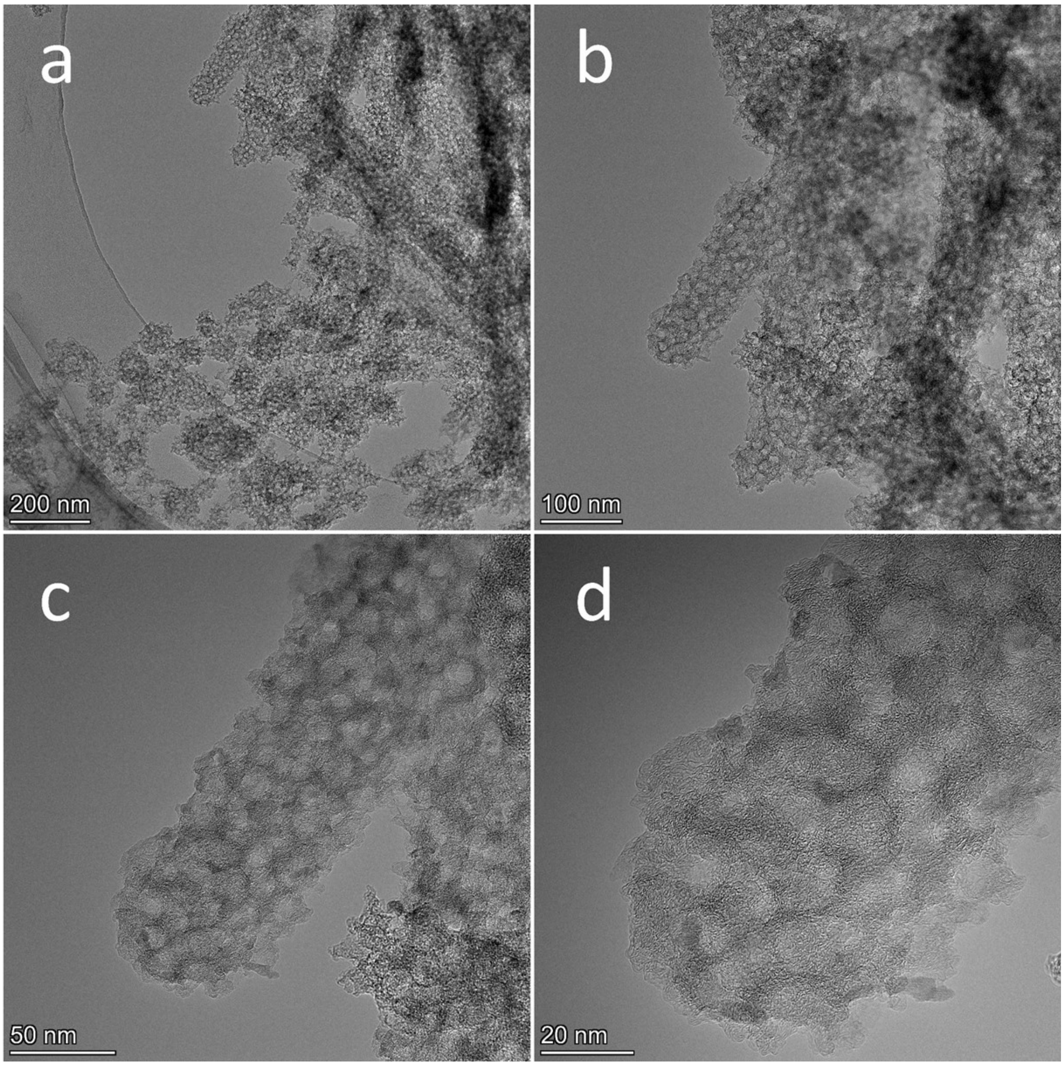

Supplementary Figure S10. TEM (**a, b**) and HRTEM (**c**, **b**) images of Meso Fe-SACs, respectively.

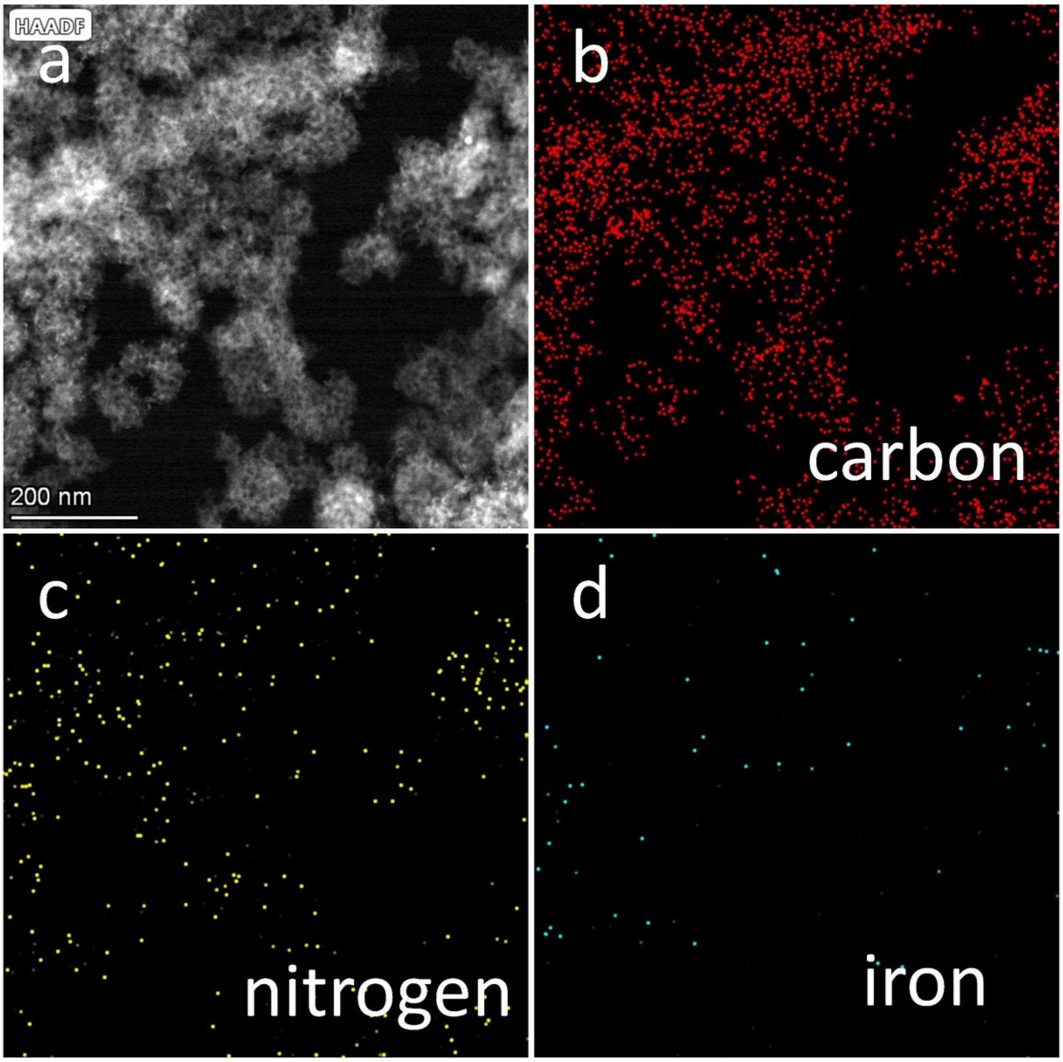

Supplementary Figure S11. High-angle annular dark-field scanning transmission electron microscope (HAADF-TEM) images of Meso Fe-SACs (**a**) and corresponding energy dispersive X-ray (EDX) mapping for Carbon (**b)**, nitrogen (**c)**, and iron (**d)**.

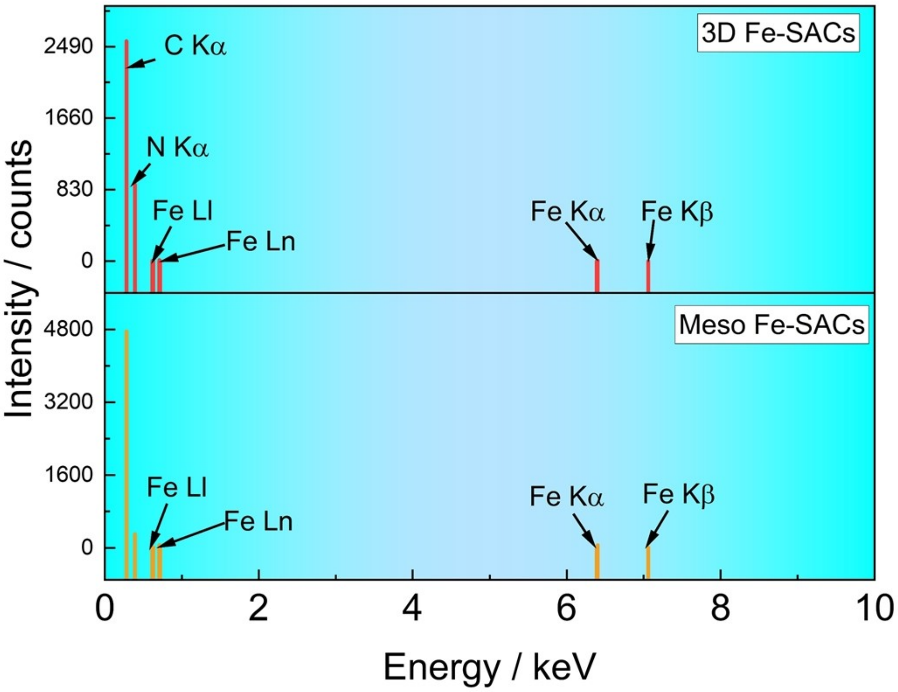

Supplementary Figure S12. EDS results of 3D Fe-SACs and Meso Fe-SACs.

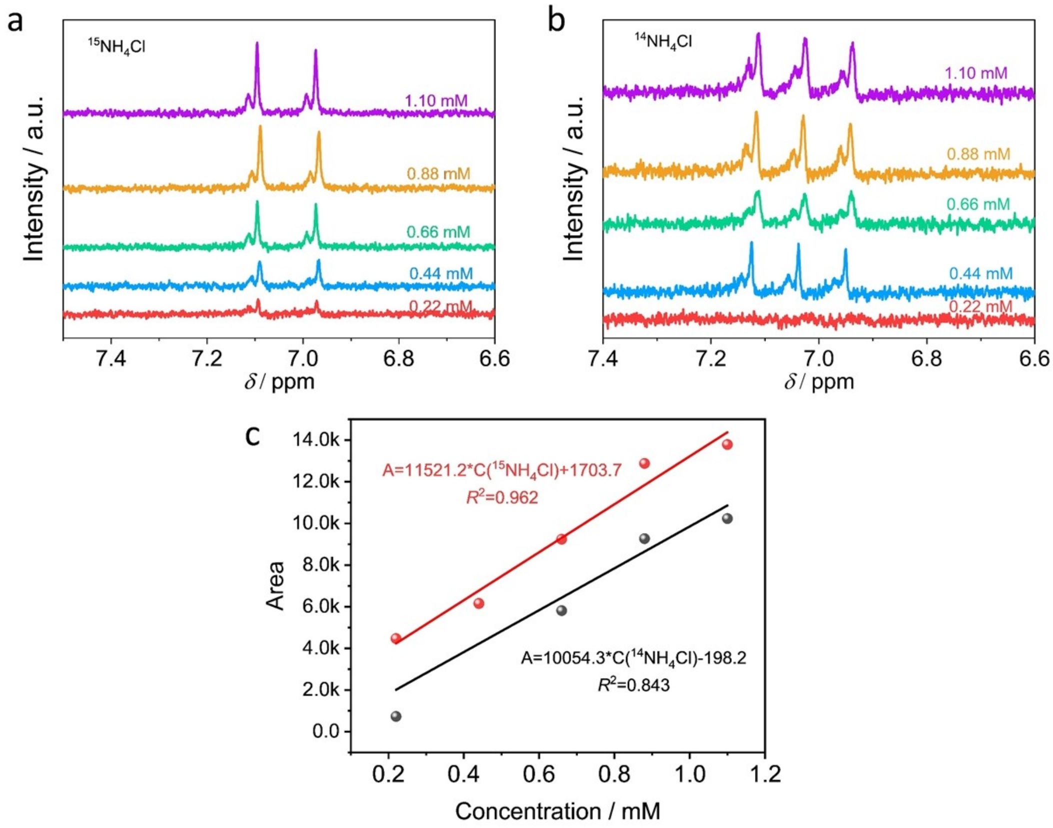

Supplementary Figure S13. **a**, ^{1}H-NMR spectra of $^{15}NH_4Cl$ standard solution at increasing concentrations in the range of 2-10 mM. **b** ^{1}H-NMR spectra of $^{14}NH_4Cl$ standard solution at increasing concentrations in the range of 2-10 mM. **c**, Corresponding calibration curve obtained from the integration of the NMR signals.

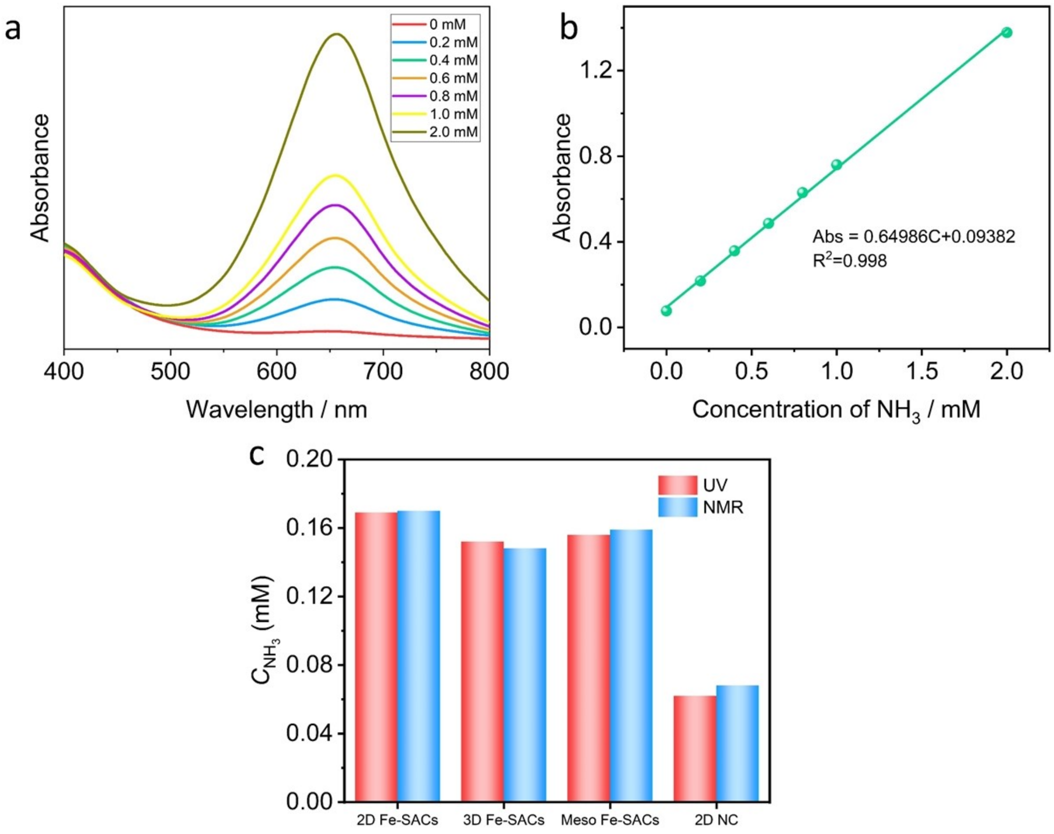

Supplementary Figure S14. **a**, the UV-visible absorption spectra of NH_4Cl at increasing concentrations in the range of 2-10 mM. **b**, Calibration curve of NH_4^+ ions present in the standard solutions. The absorbance at 654.5 nm corresponding to the peak of the ammonia was measured to estimate the ammonia concentration in the solutions The calibration curve showed a strictly linear relationship between absorbance and the NH_4^+ concentration over a large range of concentration from 0.3 to 3.0 mM. The ammonia concentration can be estimated using Equation 24:

$$Abs = 0.64986 \times \left[NH_4^+\right] + 0.09382, R^2 = 0.998\#(24)$$

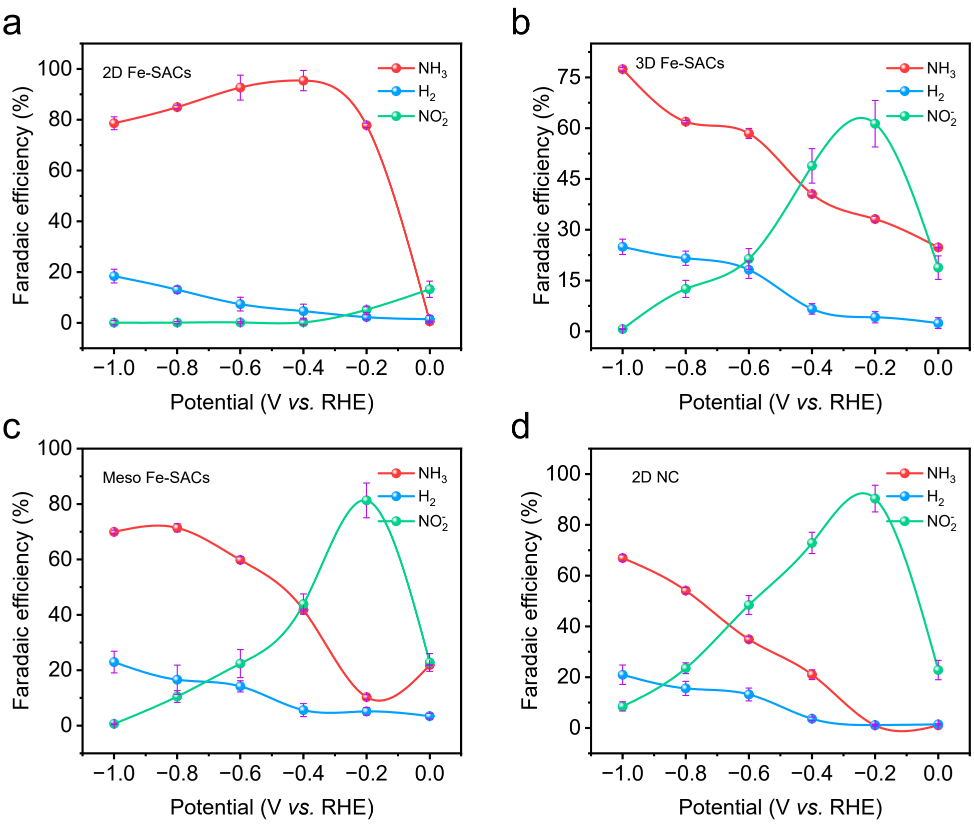

Supplementary Figure S15. Potential-dependent products distribution on 2D Fe-SACs nanosheets, 3D Fe-SACs, Meso Fe-SACs, and 2D NC nanosheets.

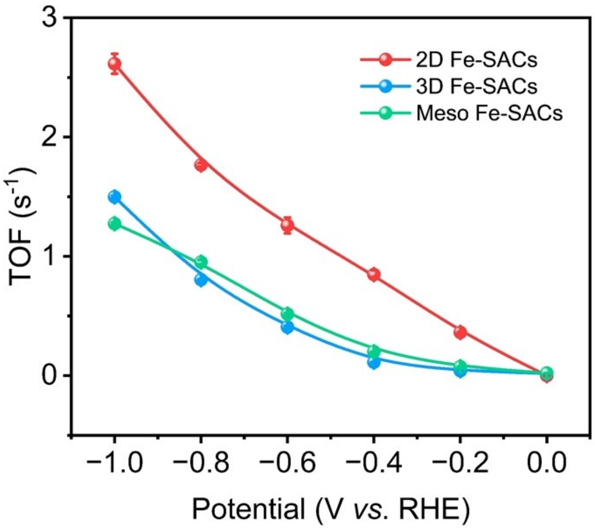

Supplementary Figure S16. Evolution of the TOF with the applied potential for the 2D Fe-SACs, 3D Fe-SACs, and Meso Fe-SACs.

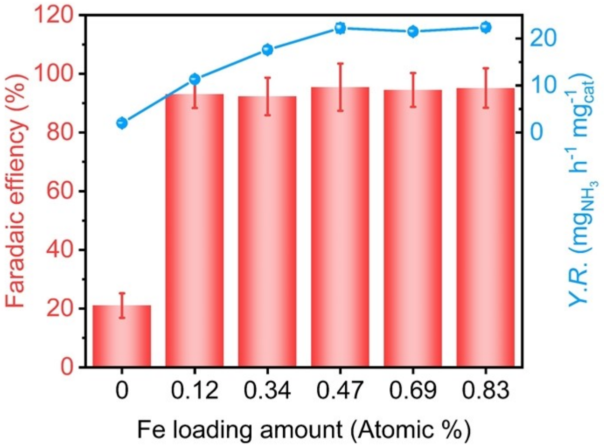

Supplementary Figure S17. Influence of the Fe loading amount in the 2D Fe-SACs catalysts on the Faradaic efficiency and yield rate for ammonia. The measurements were carried out in a 0.1 M electrolyte solution at an applied potential of -0.4 V *versus* the reversible hydrogen electrode (*vs*. RHE).

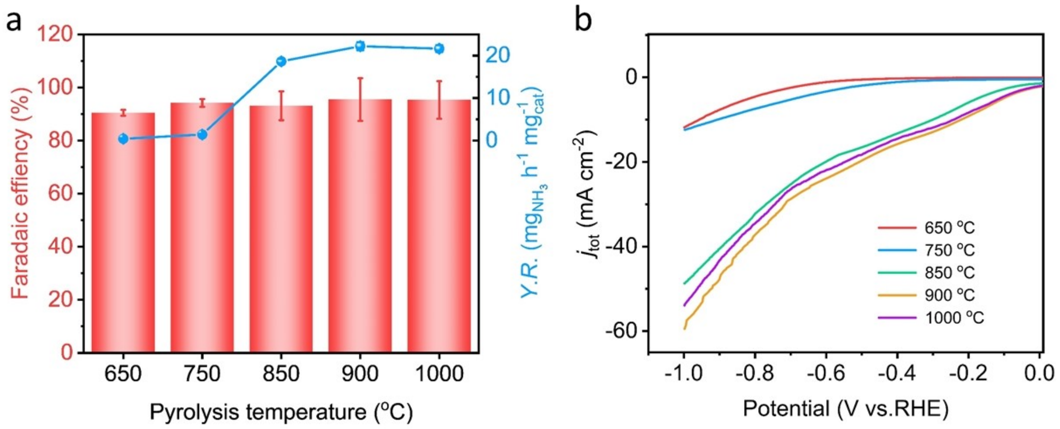

Supplementary Figure S18. **a**, Influence of the pyrolysis temperature during 2D Fe-SACs catalysts preparation on the Faradaic efficiency and yield rate for ammonia. The measurements were carried out in a 0.1 M electrolyte solution at an applied potential of -0.40 V *versus* the reversible hydrogen electrode (*vs*. RHE). **b**, Corresponding linear scanning voltammetry (LSV) curves measured in the presence of 0.1 M KNO_3.

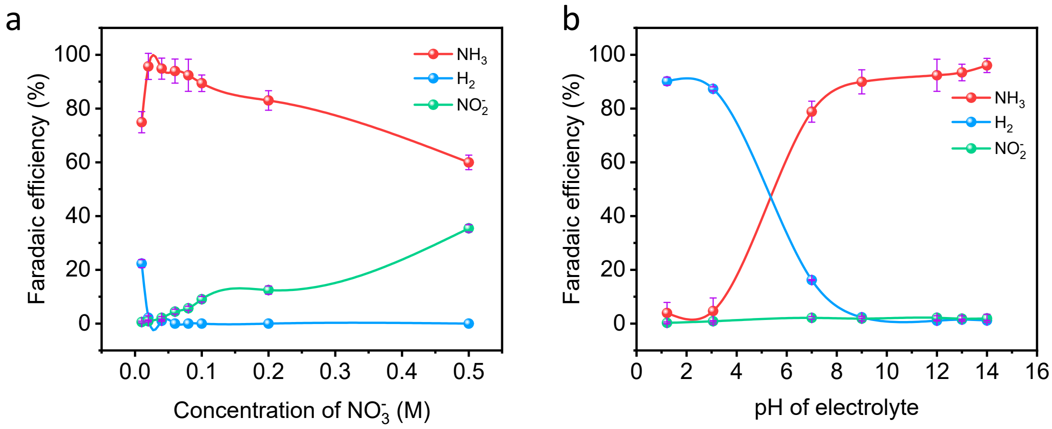

Supplementary Figure S19. Comparison of the Faradic efficiency for ammonia on the 2D Fe-SACs, 3D Fe-SACs, Meso Fe-SACs, and 2D NC nanosheets at different nitrate concentrations (**a**) and pH of electrolyte (**b**) measured at an applied potential of -0.40 V *vs.* RHE.

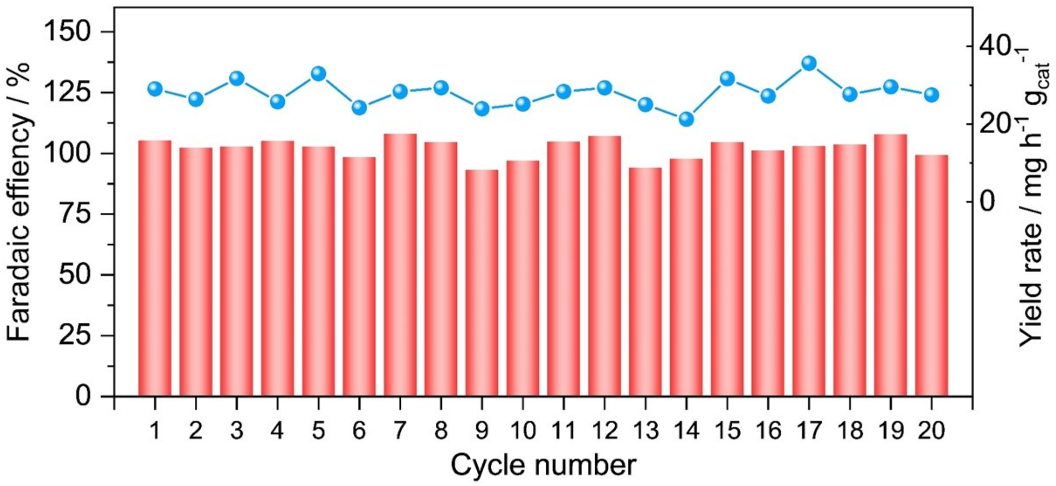

Supplementary Figure S20. Evolution of the Faradaic efficiency of 2D Fe-SACs at -0.40 V over 20 cycles of 1 hour. The electrolyte was refreshed for every cycle.

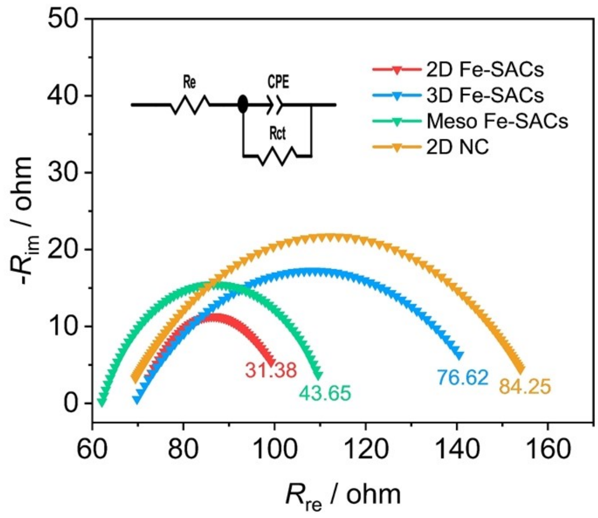

Supplementary Figure S21. Nyquist plots for 2D Fe-SACs nanosheets, 3D Fe-SACs nanosheets, Meso Fe-SACs nanosheets, and 2D NC nanosheets. The EIS was performed at an onset potential of -0.5 V vs. RHE from 100 000 Hz and 100 Hz.

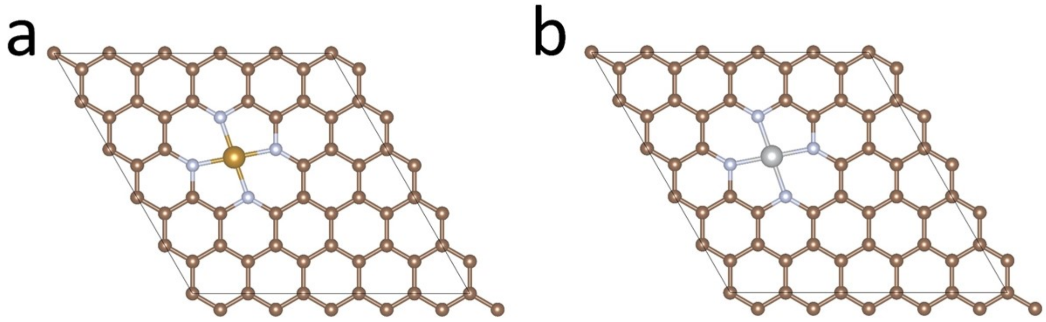

2D Fe-SACs

2D Co-SACs

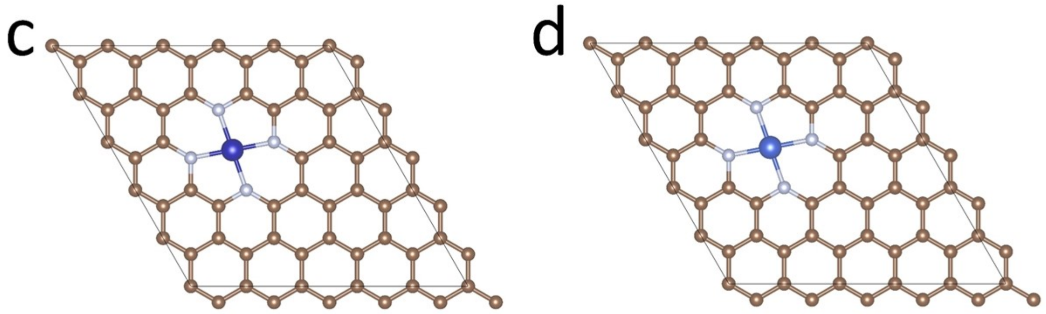

2D Ni-SACs

2D Cu-SACs

Supplementary Figure S22. Top view of various 2D single-atom transition metal catalysts nanosheets (**a** 2D Fe-SACs, **b** 2D Co-SACs, **c** 2D Ni-SACs, and **d** 2D Cu-SACs).

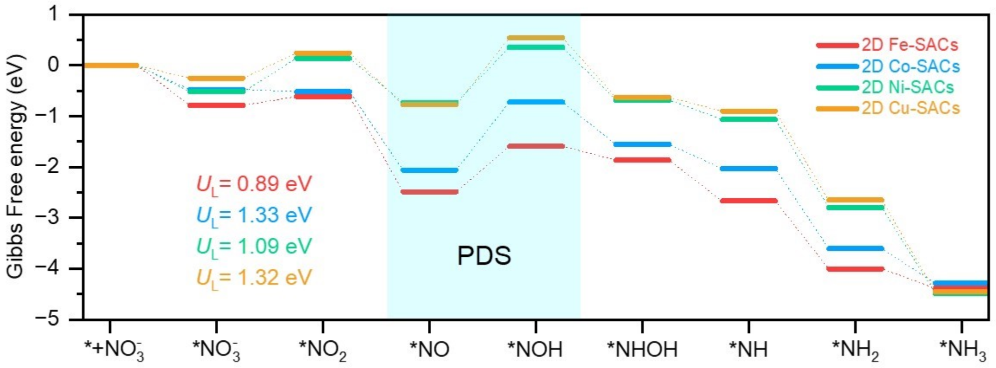

Supplementary Figure S23. Gibbs free energy diagram of NO3RR on 2D M-SACs nanosheets (M: Fe, Co, Ni, and Cu, respectively) *via* *NO→*NOH→*NHOH pathway.

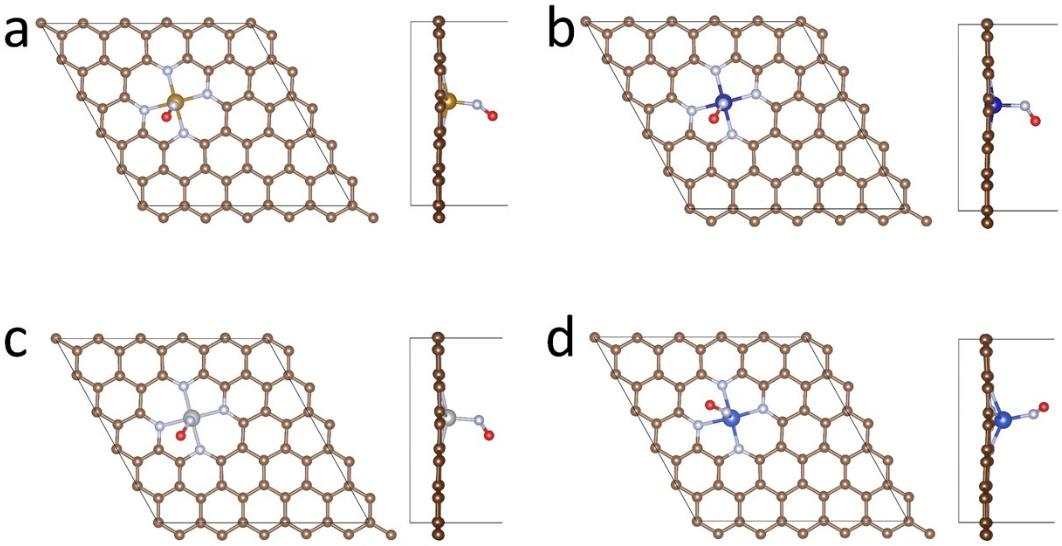

Supplementary Figure S24. Top and side views of the structure of NO adsorbed on 2D Fe-SACs (**a**), 2D Co-SACs (**b**), 2D Ni-SACs (**c**), and 2D Cu-SACs (**d**), respectively.

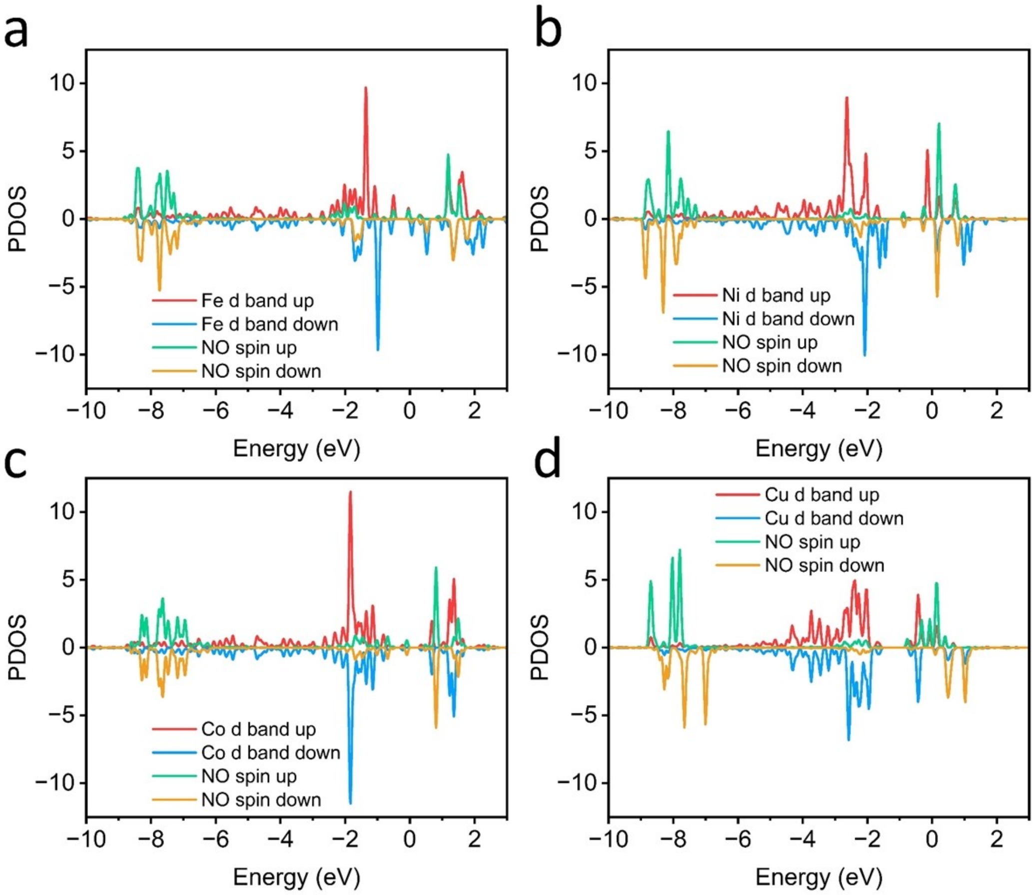

Supplementary Figure S24. Projected density of states (PDOS) of NO adsorbed on 2D Fe-SACs (**a**), 2D Co-SACs (**b**), 2D Ni-SACs (**c**), and 2D Cu-SACs (**d**), respectively.

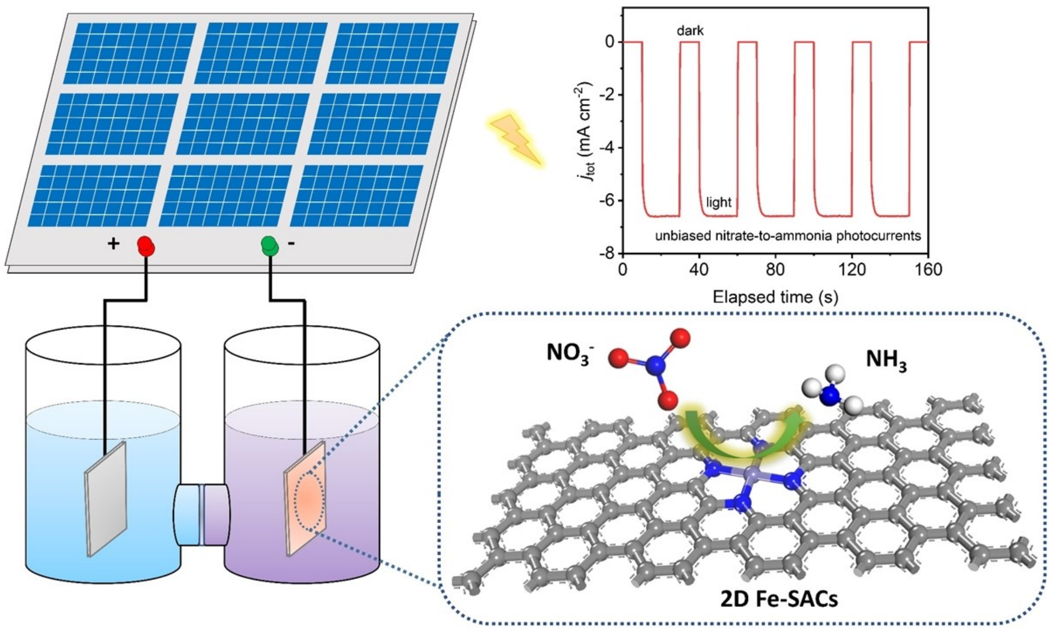

Supplementary Figure S25. Schematic of the photovoltaic-electrolysis system for the conversion of nitrate to ammonia. And current density–time curve of the PV-EC system without external bias under chopped simulated AM 1.5G 100 mW cm^{-2} illumination.

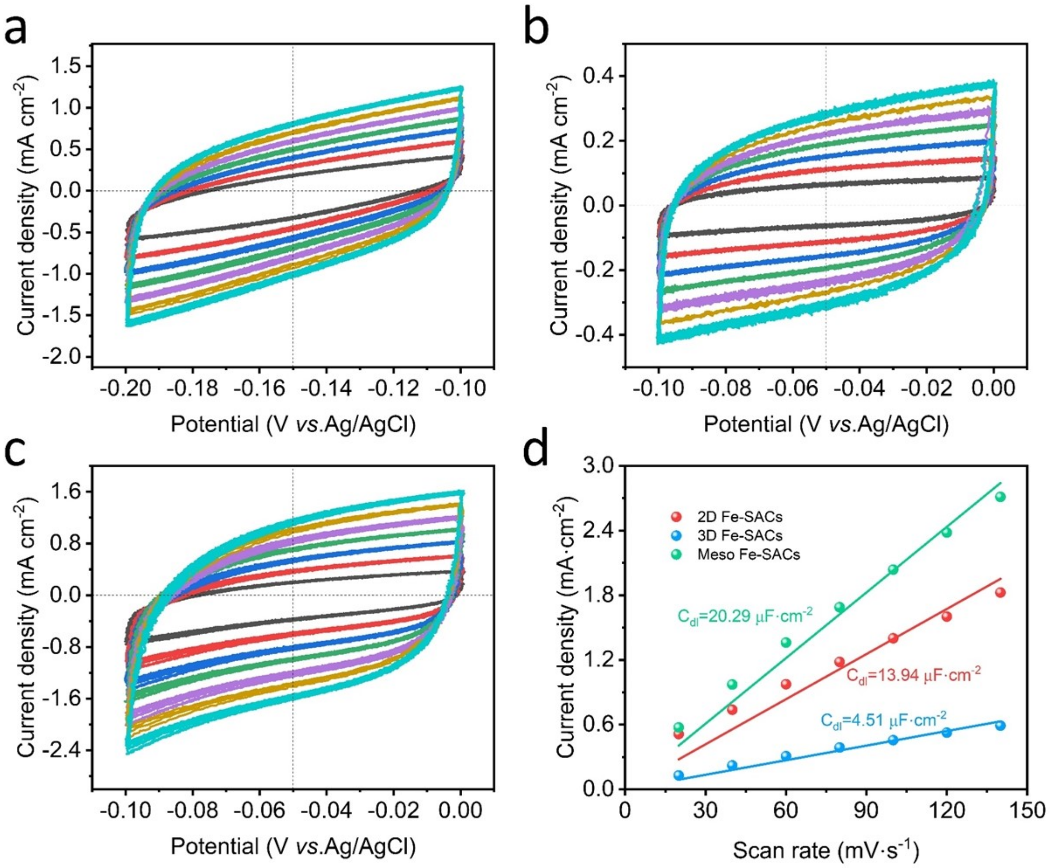

Supplementary Figure S26. Electrochemical double-layer capacitance (EDLC) measurements for 2D Fe-SACs, 3D Fe-SACs, and Meso Fe-SACs catalysts.

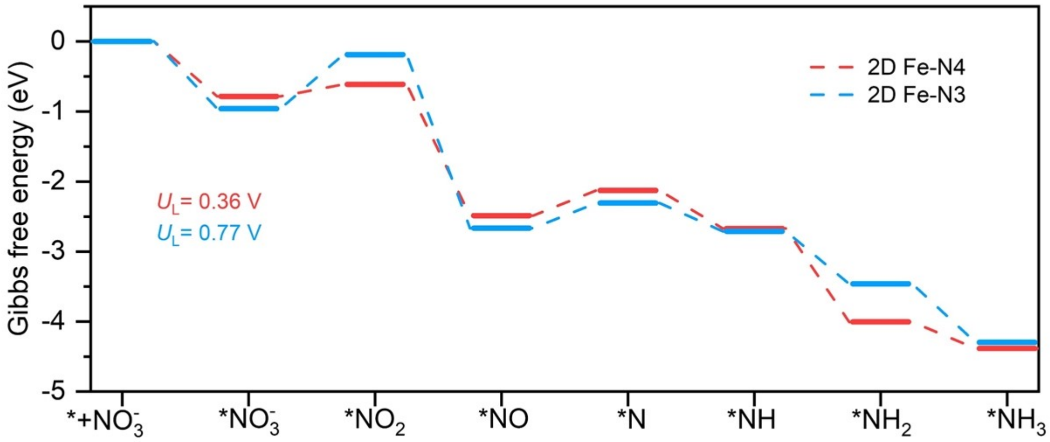

Supplementary Figure S27. Reaction Gibbs free energies for different intermediates on 2D Fe-N4 and 2D Fe-N3 nanosheets.

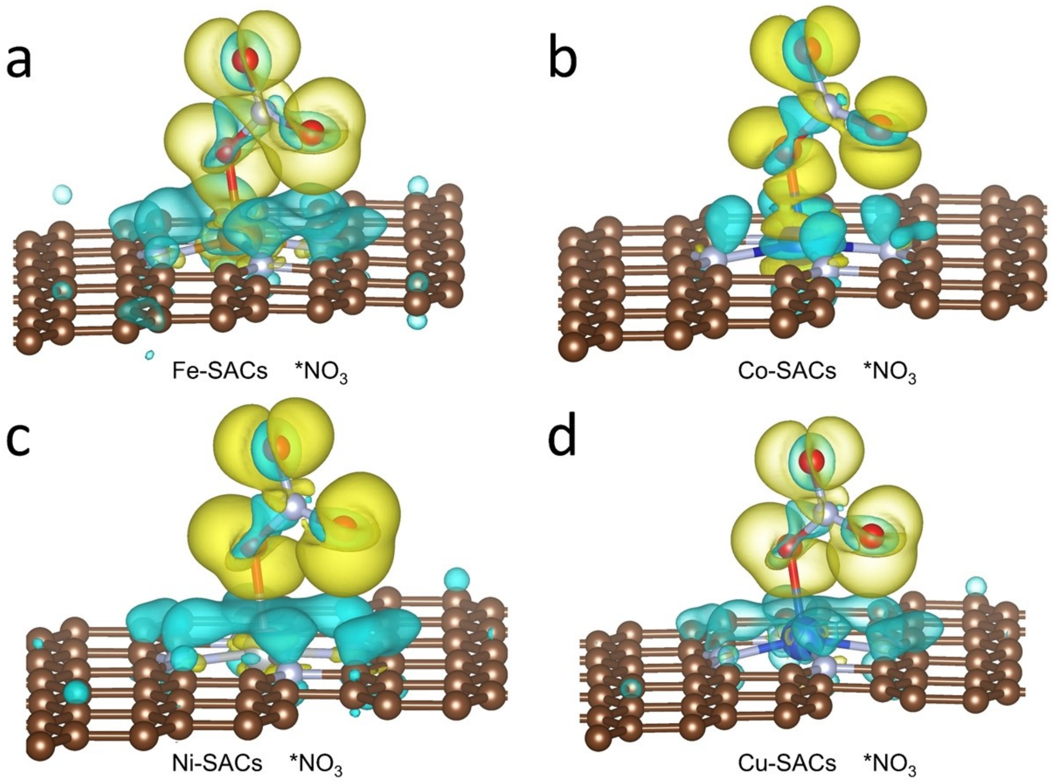

Supplementary Figure S28. Charge density difference plots for NO_3^- adsorbed on 2D Fe-SACs, 2D Co-SACs, 2D Ni-SACs, and 2D Cu-SACs nanosheets. The yellow (blue) distribution corresponds to charge accumulation (depletion).

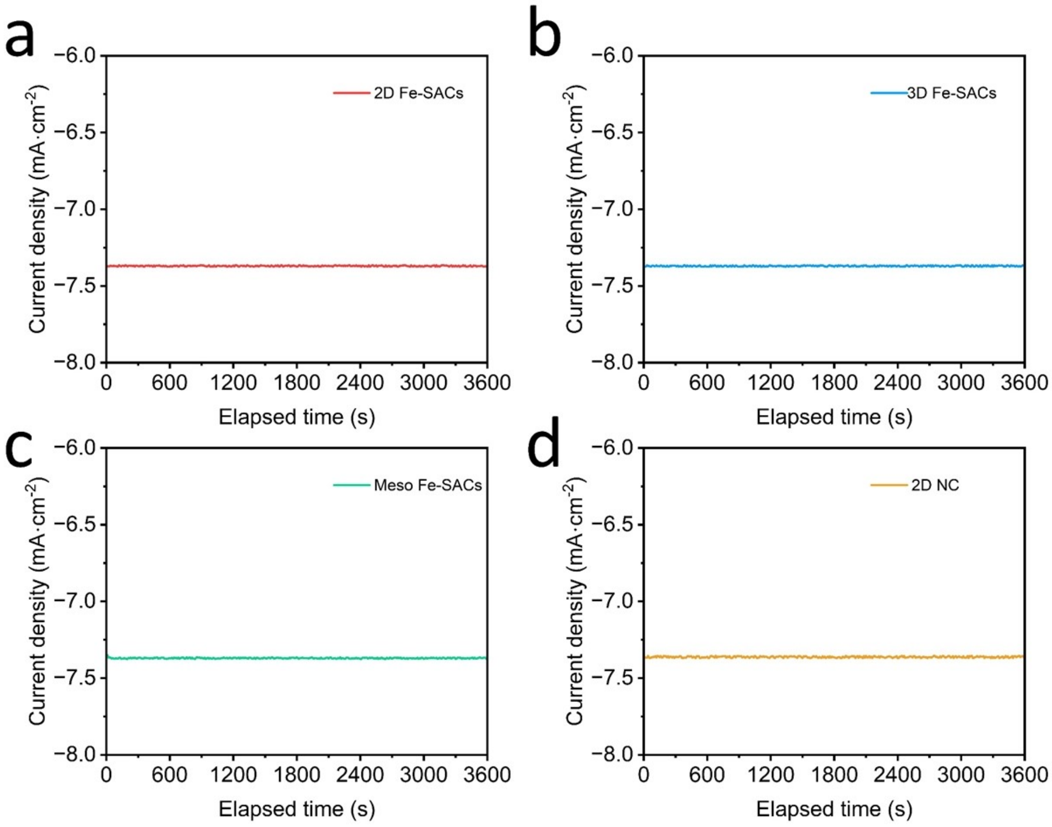

Supplementary Figure S29. Current density–time curve of the PV-EC system without external bias under chopped simulated AM 1.5G 100 mW cm^{-2} illumination. 2D Fe-SACs (**a**), 3D Fe-SACs (**b**), Meso Fe-SACs (**c**), and 2D NC (**d**), respectively.

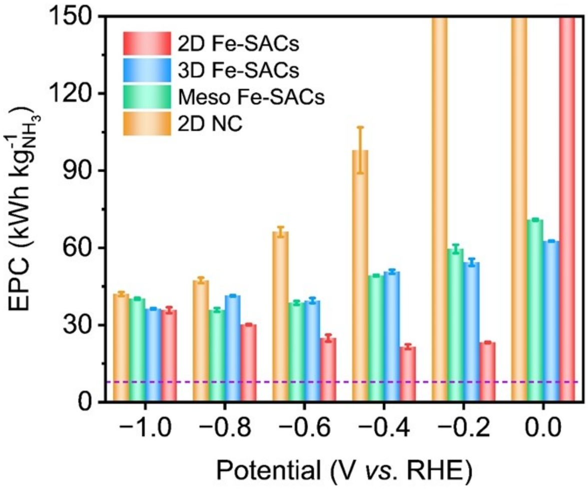

Supplementary Figure S30. Potential-dependent electric power consumption of ammonia on 2D Fe-SACs, 3D Fe-SACs, Meso Fe-SACs, and 2D NC, respectively.

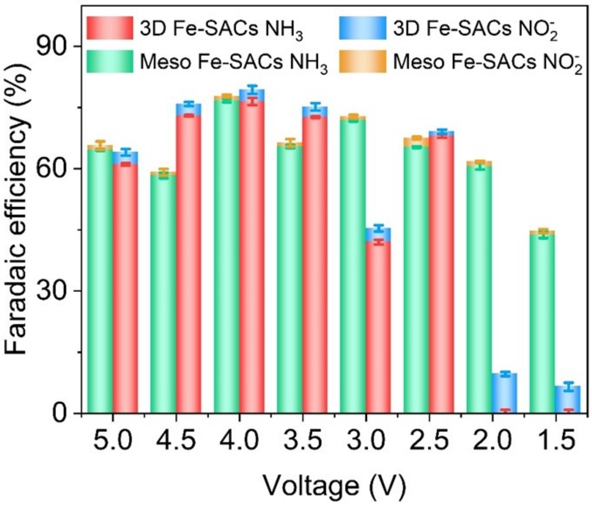

Supplementary Figure S31. Potential-dependent Faradaic efficiency of ammonia and nitrite on 2D Fe-SACs, 3D Fe-SACs, Meso Fe-SACs, and 2D NC, respectively.

Supplementary information Table S1. EXAFS fitting parameters at the Fe K-edge for various samples

Sample	Shell	N [a]	R (Å) [b]	σ^2 (Å^2·10^{-3}) [c]	ΔE0 (eV) [d]	*R* factor (%)
2D Fe-SACs	Fe-N	3.7	1.96	2.8	-1.4	0.3

[a] *N*: coordination numbers; [b] *R*: bond distance; [c] σ^2: Debye-Waller factors; [d] ΔE_0: the inner potential correction. *R* factor: goodness of fit. *S*02 was set as 0.85 for Fe-N, which was obtained from the experimental EXAFS fit of reference FePc by fixing CN as the known crystallographic value and was fixed to all the samples.

Supplementary information Table S2. Summary of the representative reports on eNO3RR performances using single-atom catalysts.

Sample	Potential (V *vs.* RHE)	Yield rate	FE [%]	pH	Nitrate concentration	Refs.
2D Fe-SACs	-0.4	1.1 mg h^{-1} cm^{-2}	95.4	13	0.1 M	This work
BCN-Cu	-0.6	3358 μg h^{-1} cm^{-2}	97.4	13	0.1 M	[15]
Cu-cis-N_2O_2	-1.2	27.84 mg h^{-1} cm^{-2}	~85	7	1000 ppm	[16]
Cu-N-C	-1	4.5 mg h^{-1} cm^{-2}	84.7	13	0.1 M	[17]
Fe SACs	-0.85	0.46 mmol h^{-1} cm^{-2}	75	7	0.5 M	[18]
Fe-MoS_2	-0.48	431.8 μg h^{-1} cm^{-2}	98	13	0.1 M	[19]
Bi_1Pd	-0.6	33.8 mg h^{-1} cm^{-2}	100	14	0.1 M	[20]
Rh@Cu	-0.2	1.27 mmol h^{-1} cm^{-2}	93	11.5	0.1 M	[21]
FeN_2O_2	-0.7	46 mg h^{-1} mg_{cat}^{-1}	92	7	0.5 M	[22]
Fe_1-NC	-0.9	18.8 mg h^{-1} mg_{cat}^{-1}	86	7	0.5 M	[23]
Fe-PPy SACs	-0.7	2.75 mg h^{-1} cm^{-2}	~100	13	0.1 M	[24]

Supplementary information Table S3. The fitting results of electrochemical activity surface area of three Fe single-atom catalysts.

Sample	Cdl (mF cm^{-2})	$EDLC_{graphene}$ (μF cm^{-2})	ECSA
2D Fe-SACs	13.94	~21[25]	663.8
3D Fe-SACs	4.51	~21[25]	214.7
Meso Fe-SACs	20.29	~21[25]	966.2

Supplementary information Table S4. The structure of *NO intermediate adsorbed on different 2D single-atom catalysts via DFT calculation.

Catalysts	**N-O bond length（Å）**	**M-N bond length（Å）**	**Charge transfer |e|**
2D Fe-SACs	1.19507	1.68782	0.40954
2D Co-SACs	1.19284	1.80786	0.24464
2D Ni-SACs	1.18756	1.80749	0.22849
2D Cu-SACs	1.19124	1.82437	0.27778

Reference

[1] L. Huang, X. Zhang, Y. Han, Q. Wang, Y. Fang, S. Dong, *J Mater Chem A Mater* **2017**, *5*, 18610–18617.

[2] D. Zhu, L. Zhang, R. E. Ruther, R. J. Hamers, *Nat Mater* **2013**, *12*, 836–841.

[3] K. M. Miranda, M. G. Espey, D. A. Wink, *Nitric Oxide* **2001**, *5*, 62–71.

[4] G. Gurudayal, J. Bullock, D. F. Srankó, C. M. Towle, Y. Lum, M. Hettick, M. C. Scott, A. Javey, J. Ager, *Energy Environ Sci* **2017**, *10*, 2222–2230.

[5] I. M. Indrupskiy, Y. Cherneva, *J Electrochem Soc* **2020**, *167*, 044508.

[6] P. Li, Z. Jin, Z. Fang, G. Yu, *Energy Environ Sci* **2021**, *14*, 3522–3531.

[7] Z. Chen, T. Wang, B. Liu, D. Cheng, C. Hu, G. Zhang, W. Zhu, H. Wang, Z. J. Zhao, J. Gong, *J Am Chem Soc* **2020**, *142*, 6878–6883.

[8] G. Kresse, J. Hafner, *Phys Rev B* **1993**, *47*, 558–561.

[9] G. Kresse, J. Hafner, *Phys Rev B* **1993**, *48*, 13115–13118.

[10] S. Grimme, *J Comput Chem* **2006**, *27*, 1787–1799.

[11] J. K. Nørskov, J. Rossmeisl, A. Logadottir, L. Lindqvist, J. R. Kitchin, T. Bligaard, H. Jónsson, *Journal of Physical Chemistry B* **2004**, *108*, 17886–17892.

[12] B. Ravel, M. Newville, in *J Synchrotron Radiat*, International Union Of Crystallography, **2005**, pp. 537–541.

[13] D. C. Koningsberger, R. Prins, **1988**.

[14] J. J. Rehr, R. C. Albers, *Rev Mod Phys* **2000**, *72*, 621–654.

[15] X. Zhao, X. Jia, Y. He, H. Zhang, X. Zhou, H. Zhang, S. Zhang, Y. Dong, X. Hu, A. V. Kuklin, G. V. Baryshnikov, H. Ågren, G. Hu, *Appl Mater Today* **2021**, *25*, 101206.

[16] X. F. Cheng, J. H. He, H. Q. Ji, H. Y. Zhang, Q. Cao, W. J. Sun, C. L. Yan, J. M. Lu, *Advanced Materials* **2022**, *34*, 2205767.

[17] J. Yang, H. Qi, A. Li, X. Liu, X. Yang, S. Zhang, Q. Zhao, Q. Jiang, Y. Su, L. Zhang, J. F. Li, Z. Q. Tian, W. Liu, A. Wang, T. Zhang, *J Am Chem Soc* **2022**, *144*, 12062–12071.

[18] Z. Y. Wu, M. Karamad, X. Yong, Q. Huang, D. A. Cullen, P. Zhu, C. Xia, Q. Xiao, M. Shakouri, F. Y. Chen, J. Y. (Timothy) Kim, Y. Xia, K. Heck, Y. Hu, M. S. Wong, Q. Li, I. Gates, S. Siahrostami, H. Wang, *Nat Commun* **2021**, *12*, 1–10.

[19] J. Li, Y. Zhang, C. Liu, L. Zheng, E. Petit, K. Qi, Y. Zhang, H. Wu, W. Wang, A. Tiberj, X. Wang, M. Chhowalla, L. Lajaunie, R. Yu, D. Voiry, *Adv Funct Mater* **2022**, *32*, 2108316.

[20] K. Chen, Z. Ma, X. Li, J. Kang, D. Ma, K. Chu, *Adv Funct Mater* **2023**, *33*, 2209890.

[21] H. Liu, X. Lang, C. Zhu, J. Timoshenko, M. Rüscher, L. Bai, N. Guijarro, H. Yin, Y. Peng, J. Li, Z. Liu, W. Wang, B. R. Cuenya, J. Luo, *Angewandte Chemie International Edition* **2022**, *61*, e202202556.

[22] W. Da Zhang, H. Dong, L. Zhou, H. Xu, H. R. Wang, X. Yan, Y. Jiang, J. Zhang, Z. G. Gu, *Appl Catal B* **2022**, *317*, 121750.

[23] L. Liu, T. Xiao, H. Fu, Z. Chen, X. Qu, S. Zheng, *Appl Catal B* **2023**, *323*, 122181.

[24] P. Li, Z. Jin, Z. Fang, G. Yu, *Energy Environ Sci* **2021**, *14*, 3522–3531.

[25] T. Zheng, K. Jiang, N. Ta, Y. Hu, J. Zeng, J. Liu, H. Wang, *Joule* **2019**, *3*, 265–278.